nature astronomy

LETTERS

https://doi.org/10.1038/s41550-020-1197-x

Check for updates

Lunar regolith and substructure at Chang'E-4 landing site in South Pole–Aitken basin

Jinhai Zhang[1,10], Bin Zhou[2,10], Yangting Lin[1]✉, Meng-Hua Zhu[3,10], Hanjie Song[4], Zehua Dong[2], Yunze Gao[2], Kaichang Di[5], Wei Yang[1], Hongyu Lin[6], Jianfeng Yang[7], Enhai Liu[8], Lei Wang[4], Yi Lin[1], Chao Li[1], Zongyu Yue[5], Zhenxing Yao[1] and Ziyuan Ouyang[9]

The South Pole–Aitken (SPA) basin is the oldest and largest impact structure on the Moon, and it gives particular insight on the lunar interior composition[1–3]. However, the surface of the SPA basin has been substantially modified by consequent impacts and basalt flooding. The exploration of the surficial material and the substructure of the SPA basin is one of the main scientific goals of the Chinese spacecraft Chang'E-4 that landed in the Von Kármán crater inside the SPA basin[4,5]. Here we report the lunar penetrating radar profiles along the track of the lunar rover Yutu-2, which show a three-unit substructure at the landing site. The top unit consists of the ~12-m-thick lunar regolith and ~120 m multilayered ejecta that were delivered from several adjacent craters. The middle unit is the mare basalts filling the Von Kármán crater. The lowest unit is another ejecta layer with a thickness of ≥200 m, likely from the Leibnitz crater. These discoveries fully support the local stratigraphy and geological explanation presented previously[6]. Our results reveal that the surface materials at the Chang'E-4 landing site are unambiguously dominated by the ejecta from the Finsen crater with a minor contribution from other neighbouring craters. The regolith measured by Yutu-2 is representative of the initial lunar deep interior materials, rather than the later erupted basalts.

The subsurface structure of the Moon preserves clues on the lunar early history but it is still poorly understood. The Apollo 17 and Kaguya spacecraft conducted radar observation to detect the global portraits of the subsurface[7–9]; however, the orbital radar measurements have relatively low resolution, and the local structures, especially the shallow fine structures, are not well known. Most studies have focused on the thickness of the so-called lunar regolith, a fine-grained layer globally covering the surface of the Moon[10,11]. The lunar regolith thickness has been investigated by in situ drilling[12], microwave remote sensing[13,14], and topography and spectral statistics of small crater ejecta[15–17], with a range from ~2 m in the young lunar maria to more than 10 m on the old highlands[12]. The Chang'E-3 mission conducted the first in situ lunar penetrating radar (LPR) detection in the Imbrium basin on the nearside of the Moon in 2013, which showed the detailed substructures of lunar regolith, multilayered ejecta and breccia of underlying bedrock, substantially improving our understanding of the Moon's surface evolution and volcanic eruption history at the landing site[18,19]. However, the subsurface structures of the Moon's farside are still unclear so far, in particular for the floor of the South Pole–Aitken (SPA) basin, the formation of which is thought to have excavated out deep materials down to the lower crust or upper mantle of the Moon.

The Von Kármán crater is filled by thick mare basalts and surrounded by several large craters (for example, the Finsen, Alder, Von Kármán L and L′, and Leibnitz craters; see Extended Data Fig. 1). The LPR onboard lunar rover Yutu-2 emitted two-frequency electromagnetic waves (that is, 60 MHz and 500 MHz) towards the lunar subsurface. The low-frequency channel (60 MHz, channel 1) has a spatial resolution of ~10 m and the maximum detection depth is ~500 m; the high-frequency channel (500 MHz, channel 2) has a spatial resolution of ~30 cm, but with a shallow detection depth of ~50 m. The amplitude of the reflections is proportional to the contrast of dielectric constants of the lunar regolith or rocks, which are dominated by the porosities and compositions[20–22]. Strong reflections occur at the boundaries between the regolith (fine-grained soil dominated), the ejecta layer (rock clast dominated), and the brecciated zone of bedrock and bedrocks, and within the ejecta layer and the brecciated zone of bedrock (where the rock clasts are larger than the spatial resolution of the LPR; Methods). In contrast, no or weak reflections occur within the fine-grained regolith (except for a few of scattered rock clasts) or homogeneous basalt layers.

Within the first three lunar days, the Yutu-2 rover conducted a 163 m LPR profile along its track (Fig. 1 and Extended Data Figs. 1–3). The LPR profiles (Figs. 2 and 3) were obtained after a series of data-processing procedures, such as decoding, denoising and removing duplicative traces (Methods and Extended Data Figs. 4–6). The high-frequency LPR profile was further processed using the depth migration method (Methods), to pursue the true depths and correct shapes of the reflectors[18]. For the low-frequency LPR channel, the reflection depth was determined directly from the travel time of the signal, using the relative dielectric model at the landing site[20–22] (see the details in Methods).

Figure 2 shows the low-frequency LPR profile, in which the subsurface was mainly divided into three (high reflection, low reflection and a relatively high reflection) units according to the amplitude of the reflections. The relatively high-reflection unit at the bottom is ≥200 m thick. According to the stratigraphy at the landing site[6,23,24]

[1]Key Laboratory of Earth and Planetary Physics, Institute of Geology and Geophysics, Chinese Academy of Sciences, Beijing, China. [2]Key Laboratory of Electromagnetic Radiation and Detection Technology, Aerospace Information Research Institute, Chinese Academy of Sciences, Beijing, China. [3]State Key Laboratory of Lunar and Planetary Sciences, Macau University of Science and Technology, Macau, China. [4]National Space Science Center, Chinese Academy of Sciences, Beijing, China. [5]State Key Laboratory of Remote Sensing Science, Aerospace Information Research Institute, Chinese Academy of Sciences, Beijing, China. [6]Beijing Institute of Space Mechanics and Electricity, Beijing, China. [7]Xi'an Institute of Optics and Precision Mechanics, Chinese Academy of Sciences, Xi'an, China. [8]Institute of Optics and Electronics, Chinese Academy of Sciences, Chengdu, China. [9]Institute of Geochemistry, Chinese Academy of Sciences, Guiyang, China. [10]These authors contributed equally: Jinhai Zhang, Bin Zhou, Meng-Hua Zhu. ✉e-mail: linyt@mail.iggcas.ac.cn

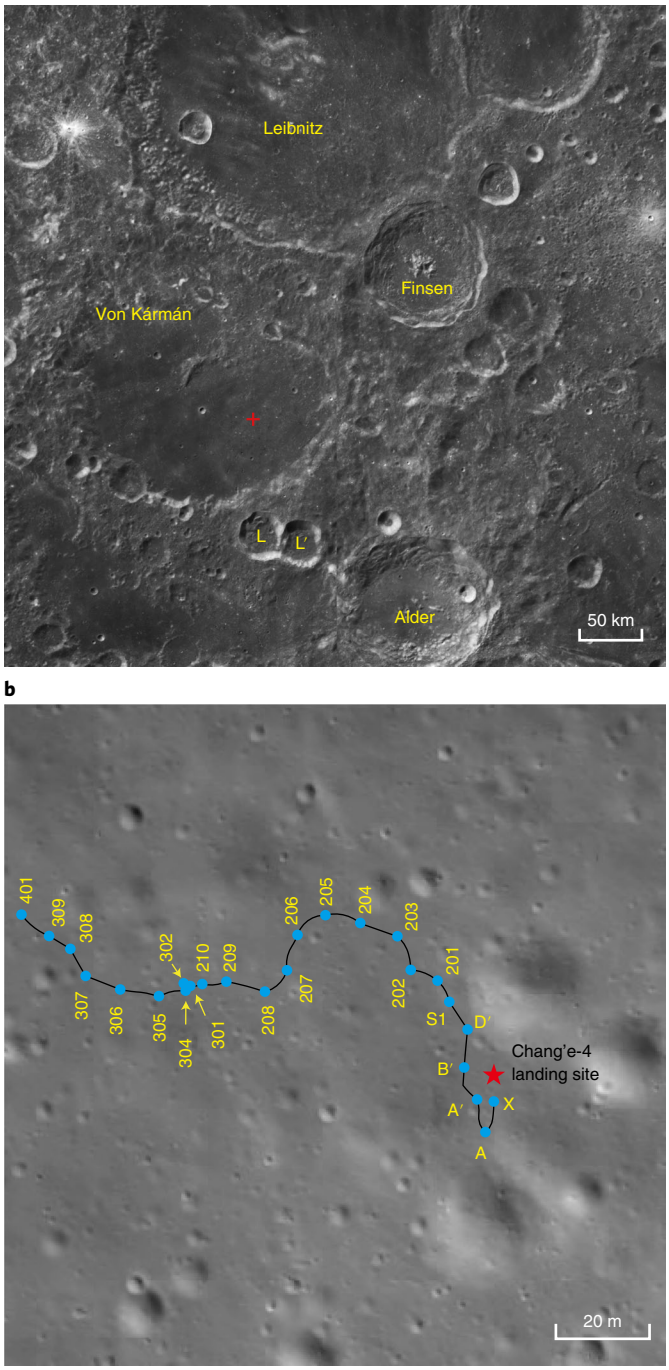

Fig. 1 | The location of the Chang'E-4 landing site and the track of the Yutu-2 rover. a, The location of the Chang'E-4 landing site at the farside of the Moon (red cross). The main craters in the area are labelled: Finsen, Alder, Leibnitz, and Von Kármán L and L′ craters. The background map was obtained by Chang'E-2 (http://moon.bao.ac.cn). **b**, The track of the Yutu-2 rover. The yellow numbers and characters are the unique name of each exploration point. The image was obtained by the descending camera under the Chang'E-4 lander. More landing site information is shown in Extended Data Fig. 1.

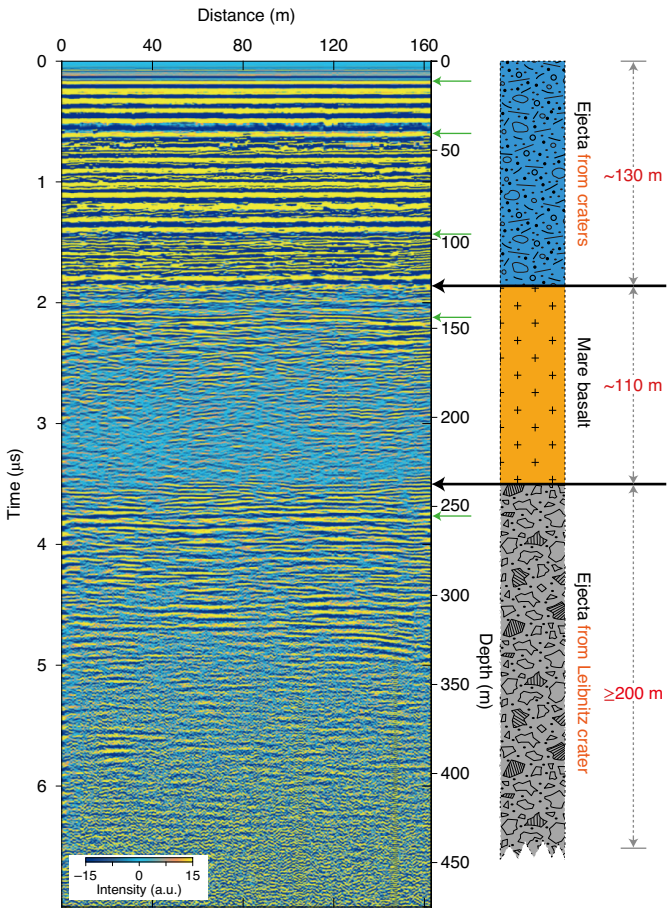

Fig. 2 | Low-frequency LPR profile along the track of the Yutu-2 rover. Left: the LPR profile obtained along the trace from the exploration point X to 401 in Fig. 1b. Right: the geological interpretation and depth estimation of each layer. The strength of the LPR reflections are denoted by the relative amplitude. The aqua colour in the LPR profile represents no or weak reflection, and the strong colour contrasts (for example, light yellow versus dark blue) denote strong reflections. In the right panel, the red number denotes the thickness of each unit and the black solid arrows show the boundaries of the three main units. The depth coordinates are converted by the lunar regolith model (Methods and Extended Data Fig. 7). The green arrows in the left panel represent the possible boundaries between sublayers with different reflection signal features. a.u., arbitrary units.

(Extended Data Fig. 2), this unit is likely from the Leibnitz crater. The numerical simulation indicates that the impact forming a Leibnitz-sized crater (~245 km in diameter) can deposit ejecta with a thickness of ~200 m at the Chang'E-4 landing site (Methods), in agreement with the thickness observed by the LPR. Therefore, this relatively high-reflection unit at the bottom is interpreted as the ejecta layer from the Leibnitz crater. The low-reflection unit, with a thickness of ~110 m in the middle, shows obviously weak reflections compared with the upper and lower units. These weak reflections are possibly from the mare basalts, because the Von Kármán crater was flooded by one or several eruptions of mare basalts that cover the ejecta of the Leibnitz crater[23,24]. The thickness of the mare basalts in the Von Kármán crater was estimated to be ~120 m from the crater shape method[25], which is well consistent with the thickness of this low-reflection unit. Thus, the low-reflection unit is deciphered as mare basalts from multiple eruptions with brief interruptions.

The LPR profiles reveal a high-reflection unit, with a total thickness of ~120 m, above the mare basalt unit (Figs. 2 and 3). This high-reflection unit appears complicated and shows obvious variation in the reflection signal features with depth (Fig. 2). Several structures with strong reflectors can be identified in the LPR profiles, likely from the crater ejecta and brecciated bedrocks.

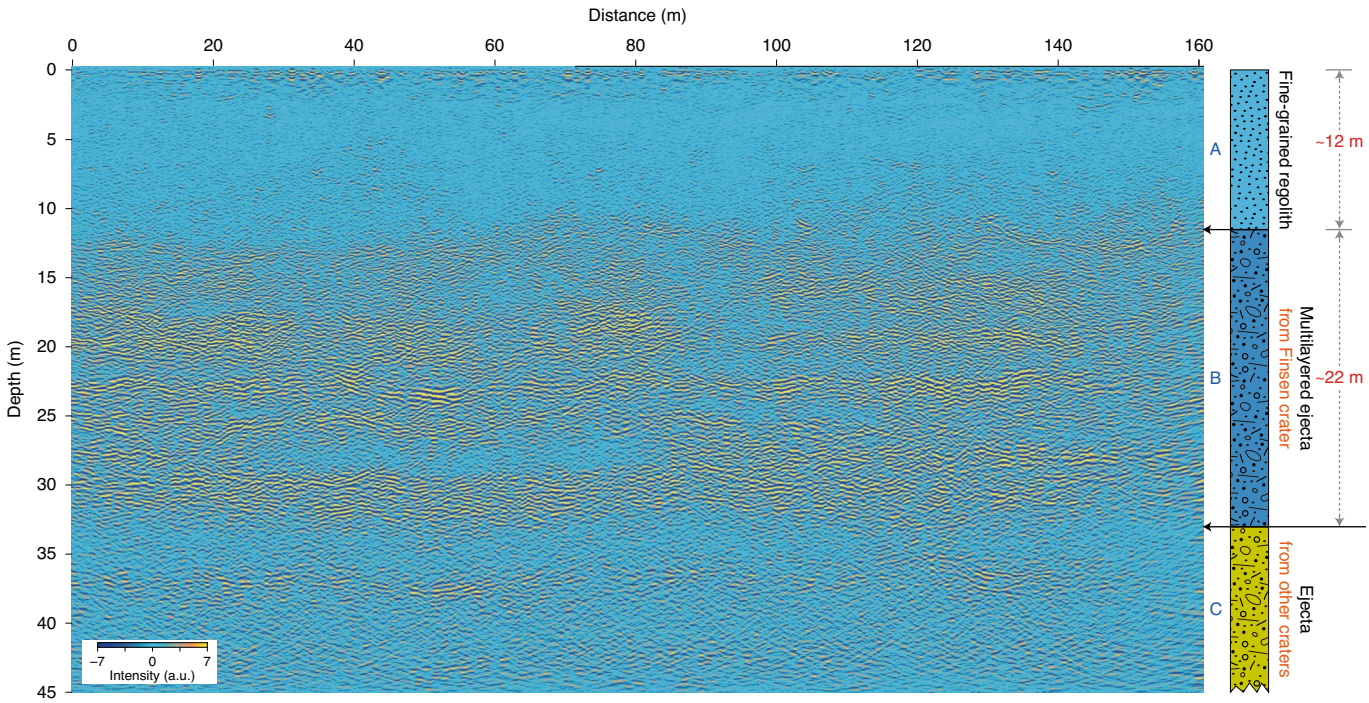

Fig. 3 | Imaging results of the high-frequency LPR using the depth migration. The function of the depth migration on recovering the true depth and shapes of the reflectors is shown in Extended Data Figs. 8 and 9. The colours, characters and numbers are the same as in Fig. 2. The fine-grained regolith (layer A) and multilayered ejecta (layer B), with a total thickness of ~34 km, are thought to be ejecta of the Finsen crater, where the upper layer (layer A) was subsequently bombarded into fine-grained regolith.

The crater ejecta was estimated to be ~70 m thick, based on the different altitudes between the landing site and the mare basalt[26]. The heterogeneity of this high-reflection unit is consistent with the regional geological context[23,24] (Extended Data Figs. 1 and 2) that several large impact craters are located around the landing site and their ejecta are deposited at the landing site. However, as the low-frequency LPR profile has a relatively low spatial resolution, we cannot connect each individual reflection unambiguously to the neighbouring crater. Instead, the detailed structures of the topmost 45 m were better revealed by the high-frequency LPR profile (Fig. 3 and Extended Data Figs. 8–10). The regolith layer (layer A) shows few reflectors, consisting of a scarcity of rocks (>30 cm) on the surface (Extended Data Fig. 3). In contrast, the underlying ejecta layer (layer B) is complicated, composed of multiple sublayers. The top sublayer is continuous and ~5 m in thickness, which shows relatively fewer scatters than the underlying ones and hence is probably indicative of the small size of rock boulders (for example, ~30 cm). Under this sublayer, there is a ~17 m sublayer with several low-reflection laminae that are discontinuous in the horizontal direction (Fig. 3). In addition, several concave areas with low reflections are also recognized (Extended Data Fig. 8b), between 15 and 30 m in depth and between 20 and 120 m in distance, probably resulting from the buried palaeocraters. Our high-frequency LPR profile shows a continuous reflection pattern around the depth of ~24 m, which was previously interpreted as the bottom of the Finsen ejecta[27]. As the Chang'E-4 mission landed on the strips radiating from the Finsen crater, we attribute both layers A and B to the ejecta of the Finsen crater. The total thickness of layers A and B is ~34 m, which is well consistent with the predicted ejecta thickness of the Finsen crater at the landing site (~30 m; Methods). The multilayered structure of the Finsen ejecta can be attributed to asteroid bombardments with a declining intensity with time, which smashed more rock boulders at shallower depths; consequently, deeper layers can preserve larger boulders due to less exposure to meteorite impacts.

The LPR profiles reveal that the heavy asteroid bombardments, thick ejecta deposits from adjacent craters and multi-episodic volcanic eruptions[28] took place within the SPA basin, by which the exposed materials of the lunar deep interior and the basin-forming impact records have been severely modified. These derived subsurface structures are well consistent with expectations of the shallow structure of the lunar upper crust[29], supporting the idea that large-scale cratering plays a substantial role in the formation of the subsurface structure of the Moon[7]. These discoveries shed light on the complex asteroid bombardment and volcanic eruption history of the SPA basin. The subsurface structures are indicative for landing-site selection in future explorations, especially for sample-return missions.

Methods

Brief introduction of the LPR. The LPR on the Yutu-2 rover of the Chang'E-4 mission is the same as that on the Yutu rover of the Chang'E-3 mission at Imbrium basin in 2013[30–32]. The LPR can image the interior of the lunar regolith and can detect the geological structure of the subsurface by analysing the electromagnetic waves reflected from the subsurface after stimulating impulsive sources. The LPR was designed to detect the subsurface structure, based on the radar signals reflected at interfaces of objects with different dielectric constants, which are determined mainly by composition (for example, FeO and TiO_2 contents) and porosity. Hence, the LPR could detect the boundaries between the porous lunar regolith, ejecta, basalt lava layers and bedrock. In addition, the lunar regolith and ejecta layers commonly contain large rock boulders (larger than the spatial resolution of the radar wave), and the signals reflected at the interfaces of these large boulders can also be detected. In contrast, homogeneous regions within the fine-grained regolith and the interior of basalt layers show weak (or even no) radar reflection.

Two broadband monopoles are chosen as the channel 1 antennas (one transmitting antenna and one receiving antenna), which are respectively mounted on two bottom sides of the lunar rover's top board, spaced about 800 mm apart. The antenna is 1,150 mm in length and 12 mm in diameter. The dominant frequency for the source of channel 1 is 60 MHz. A set of bow-tie antennas are

chosen as the channel 2 transceiver antenna, which are mounted at the bottom of the lunar rover, about 30 cm away from the ground. Each antenna element is 336 mm in length and 120 mm in width, and the space between the antenna elements is about 160 mm. Channel 2 works with a dominant frequency of 500 MHz, which penetrates shallower than channel 1 but provides a better spatial resolution. The depth resolutions of channels 1 and 2 are <10 m and <30 cm, respectively, based on the ground experiments[31]. Extended Data Fig. 1 shows the landing site of Chang'E-4 and the track of lunar rover Yutu-2.

Processing of the LPR data. An LPR profile with a total length of ~163 m was carried out in the first three lunar days by the Yutu-2 rover (Extended Data Fig. 1d). Extended Data Fig. 4a shows 1,973 traces obtained by channel 1. It is difficult to identify the deep reflections as the original data are too noisy. We reduced the random noise by applying the sixth-order Butterworth band-pass filter between 10 and 80 MHz on each trace and a two-dimensional median filter[18]. The results are shown in Extended Data Fig. 4b, where the deepest reflections that can be identified from the profile are at ~6.5 μs. According to Extended Data Fig. 5, we can determine that the time delay before the first arrival for channel 1 is about 57.5 ns, which has been removed in Extended Data Fig. 4b. The singular value decomposition[33] of the low-frequency LPR profile (Extended Data Fig. 6) further separates the reflections and diffractions. We divide the singular values into three segments according to their energy characteristics, 1–10, 11–200 and 201–1,973 (Supplementary Fig. 5), and the results correspond to the low-, band- and high-pass eigenimages (Extended Data Fig. 6b–d), which mainly present the reflections, diffractions and random noises, respectively.

It is noticed that the profile processed with the low-pass eigenimage filtering is consistent with Fig. 2, where we can again identify the two boundaries at ~130 and ~240 m, respectively. The LPR signal patterns change across both boundaries. The reflection signals gradually vanish at ~440 m (Extended Data Fig. 6b). The diffractions mainly appear in the band-pass eigenimage (Extended Data Fig. 6c) but with some energy weakening at the strong reflection zones shown in Extended Data Fig. 6b, due to energy leakage of high-frequency components during the singular value decomposition[33]; thus, we could not identify more layers from the band-pass eigenimage according to the energy pattern of diffractions. Nevertheless, the results of eigenimage filtering still confirm that the low-frequency LPR profile consists of reflections and diffractions from the underground structures, without apparent systematic artefacts over the lunar surface. Furthermore, the results of eigenimage filtering provide us with more information to confirm the rationality of the three main units divided by the two notable geological boundaries at ~130 and ~240 m shown in Fig. 2.

Channel 2 has two receiving antennas (2A and 2B) and channel 2B has recorded 4,416 high-quality traces. For detailed information on processing the data (including removing the direct currents, noise attenuation and weak signal enhancement), please refer to Zhang et al.[18]. We applied the sixth-order Butterworth filter with a band-pass between 100 and 800 MHz.

The exact coordinates of each trace are not available; thus, we assume that the rover is moving at a constant speed between two adjacent stops, and, therefore, we take a uniform spatial interval of 0.0365 m between two adjacent traces. The error is fairly small as the coordinates at some control points are well estimated (see blue dots in Extended Data Fig. 1d). The route of the Yutu-2 rover is generally horizontal, and the maximum vertical deviation from the horizontal baseline is no more than 1 m; thus, we disregard the topography of the patrol area. The effect associated with the topography can be reconsidered in the future after the coordinates of all traces are comprehensively estimated from other methods[34].

Verifying the function of depth migration. Seismic exploration has developed many advanced techniques to detect terrestrial reservoirs buried under complex deep substructures, such as signal processing and seismic migration that are essential for extracting weak signals and high-accuracy imaging of substructures[35,36]. These methods have been applied to process the LPR data obtained by Chang'E-3[18].

In general, each underground scattering object would be mapped into a hyperbola in the profile due to the wave propagation effects; thus, it is difficult to identify substructures directly from the ground-based profile. Therefore, the depth migration is crucial for imaging complex structures using the reflected seismic waves[35–38] and LPR[18]. It can reduce the propagation effects and recover both the shapes and the true depth of scattering objects. The migrated profile would be much closer to the actual position, compared with the original profile, which is important for interpreting the structures and the process of the lunar subsurface.

Zhang et al.[18] examine the detectability of several typical structures: syncline, anticline, dipping structures, circular and rectangular blocks, buried in a linear increasing gradient model of relative dielectric constant. They show that it is difficult to identify complex structures directly from the synthetic profile, as a lot of crossed hyperbolas can be observed due to wave propagation effects; in contrast, most gently dipping structures are well recovered by depth migration using the one-way wave equation method[37–39].

In this study, we can see that the depth migration, with the one-dimensional model shown in Extended Data Fig. 7, can move the hyperbolas back towards the true positions of the scattering points or reflecting interfaces, as shown in Extended Data Fig. 8. Extended Data Fig. 9 further shows some local details in the rectangles in Extended Data Fig. 8. Obviously, the migration results show much clearer scattering objects and more continuous reflectors than the original LPR profile, and most scattering objects are well imaged. Therefore, the depth migration is necessary for high-resolution imaging of the complex structures and objects buried in the lunar regolith.

Extended Data Fig. 7 shows a reasonable background model (or macro model) at the landing site, based on some prior information from lunar geological studies[12,24] and the sublayer depth estimated by the depth migration (Extended Data Fig. 8). Although a laterally homogeneous macro model was used for the depth migration, the imaging results still show many clear structures, especially for the continuous structures and scattering objects. A finer model including lateral variation would be helpful for better accuracy in relocating deep reflectors.

As pointed out by Zhang et al.[18], the narrow receiver array of the LPR (two receivers are 16 and 32 cm away from the source, respectively) leads to the difficulty in receiving the reflected waves from nearly vertical structures under the rover; thus, we would not image steep dips, as we have too weak or even no signal reflected from them. Therefore, we can faithfully identify only the upper and bottom surfaces of the objects from the migration results, as we could not observe their vertical boundaries. Nevertheless, the migration results still provide us with solid support in interpreting the lunar subsurface, as the artefacts are greatly reduced by focusing the scattering waves and by relocating the reflectors much closer to their true positions.

The relative dielectric model at the landing site. For the depth migration, we need a velocity model, at least a one-dimensional model (that is, the gradient model). The velocity of the electromagnetic waves propagating in homogeneous media can be obtained by

$$v = \frac{c}{\sqrt{\varepsilon_r}},$$

where c is the speed of light in vacuum and ε_r is the relative dielectric permittivity. The relative dielectric permittivity of the lunar regolith is nearly independent of frequency above 1 MHz and temperature[12], and it is dominantly controlled by the bulk density approximately by

$$\varepsilon_r' = 1.92^{\rho},$$

where ρ is the bulk density in g cm^{-3}, which varies with depth z (in centimetres) in a hyperbolic form[12]

$$\rho = 1.92\frac{z+12.2}{z+18}.$$

From the depth migration results (Fig. 3 and Extended Data Fig. 8b) and the low-frequency profile (Fig. 2 and Extended Data Fig. 6), we can identify several sublayers; thus, we can build up the bulk relative dielectric model of the lunar regolith and the subsurface at the Chang'E-4 landing site as follows

$$\varepsilon_r = \begin{cases} 1.92^{\rho}, & 0<z\le h \\ 4.5 \text{ for ejecta} & h<z \\ 6.0 \text{ for basalt} & h<z \end{cases},$$

where $h = 12$ m is the depth of the lunar regolith layer (Fig. 3).

We determined the model by guessing an initial model according to the geological interpretation (Figs. 2 and 3) where the ejecta or brecciated top of mare basalt have a fixed relative dielectric permittivity of 4.5 and the mare basalt has a relative dielectric permittivity of 6 (refs. [12,21,22]); then, we converted the time coordinate into the depth coordinate using a fine depth interval (0.05 m) according to $v = c/\sqrt{\varepsilon_r}$; finally, we updated the model to make sure that the depth given in the model is consistent with the depth of each geological layer in the LPR profile (Figs. 2 and 3). Our final model after several iterations is shown in Extended Data Fig. 7.

Distinguishing different layers in the LPR profiles. We distinguish different layers according two assumptions: (1) the amplitude of reflections is proportional to the contrast of dielectric parameters above and below the reflector; (2) a continuous region of reflections with a similar pattern should be interpreted as a geologic layer formed under similar conditions. We can observe two notable geological boundaries at the depths of ~130 and ~240 m (Fig. 2), which have the strongest pattern mutations in the low-frequency LPR profile; in addition, we can distinguish more layers with apparent pattern mutations in the depth migration results of the high-frequency LPR profile (Fig. 3). Lv et al. have performed comparative analyses of LPR data using numerical simulations and provided some criteria for distinguishing different layers[40], which provide more experiments and details on distinguishing different layers.

The consistency of the low-frequency channel and the high-frequency channel. Extended Data Fig. 10 shows the comparison between the low-frequency channel and the high-frequency channel. Obviously, the amplitude clipped parts in the low-frequency channel (mainly within 0.31 μs, as shown in Extended Data Fig. 5) can be well constrained by the high-frequency channel within 0.62 μs.

The uncertainty of geological interpretation. The depth coordinates are converted by the relative dielectric model (Extended Data Fig. 7), which may vary if we use a completely different model according to some new constraints. The model here is constructed after the Apollo samples[12], which is the best model we can provide. The uncertainty of the depth estimation is small at shallow depths, for example, being 11 cm at 70 cm, and it increases with the depth[18].

Numerical simulation for the impact cratering process and ejecta thickness distribution. The ejecta thickness can be described as a power function of the range x (measured from the crater centre), $T = T_{tr}(x/R)^{-b}$, where T is the estimated thickness at distance x; T_{tr} is the estimated ejecta thickness at the rim of the transient crater; R is the transient crater radius; and b is the exponent parameter within a range from 2.3 to 3.3. In this equation, both T_{tr} and b are independent unknowns. Although these two parameters can be estimated according to the experiences derived from the laboratory experiments, a small variation of the selected exponent b can substantially affect the estimation of ejecta thickness at a location far away from the crater centre. The numerical simulation allows systematic parametric studies on the effect of target properties such as porosity and strength on ejecta distribution, and therefore could provide a more precise estimate of the ejecta thickness.

In this work, we use the multi-material, multi-rheology two-dimensional iSALE (Dellen version) shock physics code[41,42] to model the impact cratering process and ejecta distribution of 200-km-diameter Leibnitz crater and 72-km-diameter Finsen crater (Supplementary Fig. 1). The iSALE is based on the SALE (Simplified Arbitrary Lagrangian Eulerian) hydrocode[43] and has been used to simulate both small-scale laboratory experiments[44] and large-scale lunar basin formation (for example, refs. [45–49]).

In our simulations, we use the analytic equation of state for dunite[50,51] to represent the composition of the impactor and the Tillotson equation of state for gabbroic anorthosite to represent the composition of the target. However, for the 200-km-diameter Leibnitz crater, its formation may have penetrated through the crust layer and excavated the deep materials. Therefore, we assume that the target of the Leibnitz crater is a crust with a thickness of ~20 km overlaying the dunite mantle material. This is reasonable because the average crustal thickness within the SPA basin is ~20 km (ref. [52]). Material strength and damage is accounted for based on the model of Collins et al.[41] and Ivanov et al.[53]. A temporary weakening model, acoustic fluidization[54,55], is also considered to facilitate collapse in the impact cratering process. The detailed parameters for the impact crater simulations are listed in Supplementary Table 1.

To generate a crater comparable in size to the Leibnitz crater, the impactor diameter was varied between 5 and 24 km. The computational domain covers an area of 300 km in the lateral and vertical directions with a cell size of 1 km × 1 km in the high-resolution zone. For the Finsen crater, we varied the impactor diameter from 5 to 24 km. The computational domain covers an area of 100 km in the lateral and vertical directions with a cell size of 0.06 km × 0.06 km in the high-resolution zone. For both impact cratering simulations, the resolution of 20 cells per projectile radius is suitable for the calculation of ejecta properties[48,56]. We varied the impact velocity between 10 and 20 km s^{-1} for both simulations to cover a suitable velocity for asteroid hitting the Moon[57,58]. These impact velocities could also represent moderately oblique incidence angles because the vertical component of the impact velocity mainly controls the diameter of the craters. In all simulations, we assigned a lunar surface gravitational acceleration of 1.62 m s^{-2}. Owing to the axisymmetric nature of the two-dimensional model, all simulations considered only vertical impacts. Though vertical impacts are highly unlikely, they provide a reasonable proxy for the most common angle of impact (45°) on planetary surfaces. In this work, we run 40 impact models in total (20 for the Leibnitz crater and 20 for the Finsen crater). All simulations were stopped at 2 h (modelling time) after impact.

We track the ejecta trajectories and physical states by using Lagrangian tracers in iSALE, which were initially placed in each computational cell and represent the matter originally in that cell throughout the simulation. We consider the tracer as ejecta that have ballistic trajectories, cross the pre-impact target surface and deposit beyond the transient crater rim. We record its launch angle and launch velocity by interpolating the nodal velocities when its trajectories interact with the pre-impact surface. Using these parameters, the parabolic trajectory of each tracer and final position were calculated[48,56]. Note, ejecta with velocities below 2.4 km s^{-1} (Moon's escape velocity) were thought to move along parabolic trajectories and could eventually fall back to the lunar surface. The surrounding surface of the crater was subdivided into discrete rings. The ejecta thickness was calculated from the number of tracers that landed at a given distance from the point of impact. This approach for the calculation of ejecta thickness has been validated against laboratory impact experiments into sand[44]. The entrainment of local material into the ejecta blanket upon landing is not taken into account. At larger distance, this process may be non-negligible[56,59]. It is noted that we do not simulate the formation of the ejecta plume in our models; vapourized material (material with a density <300 kg m^{-3}) is removed from the computational mesh to expedite simulation time. This assumes that the expanding vapour plume and small ejected fragments do not have any effect on crater formation and that the drag of the vapour on the ejected particles is negligible, which is a reasonable assumption for ejecta forming layers several hundreds of metres thick. Artemieva et al.[60] showed that only a relatively thin layer of fine-grained ejecta and dust particles interacting with the vapour plume are finally deposited on top of the ballistic ejecta.

Supplementary Fig. 2 shows the snapshots of the impact cratering process for an impactor with a diameter of 6.2 km and an impact velocity of 15 km s^{-1}. The impact produces a complex crater with a diameter of ~78 km, analogous to the size of the Finsen crater. The produced centre peak is ~2 km below the pre-impact surface, consistent with that of the Finsen crater. We calculate the average profile of topography for the Finsen crater (Supplementary Fig. 2d) from the Lunar Orbiter Laser Altimeter (LOLA) observations in a crater-centred projection over the white region of Supplementary Fig. 1. The profiles of elevation derived from the impact simulation and observations match well, suggesting that our impact model could reasonably reproduce the formation of the Finsen crater. Supplementary Fig. 3 shows the ejecta thickness as a function of radial distance from the rim of the Finsen crater to 200 km from the crater centre. The ejecta deposit near the crater rim is ~1.9 km and decreases with increasing radial distance from the crater centre. The decrease of ejecta thickness with distance can be described by a power law with an exponent of −3.2, which is consistent with laboratory experiments[44,61] and ejecta thickness observations for the lunar crater[29]. The Chang'E-4 landing site is ~138 km from the centre of the Finsen crater. According to our simulation, ~32-m-thick ejecta from the Finsen crater deposited at the Chang'E-4 landing site, which is similar to the thickness derived from the LPR (Fig. 3).

Supplementary Fig. 4a shows the structure of the simulated crater by an impactor with a diameter of 14 km and an impact velocity of 16 km s^{-1}. The structure is ~230 km in diameter, which is similar to the size of the Leibnitz crater. As the Leibnitz crater was filled by mare basalts and its morphologies have been destroyed by subsequent impacts (Supplementary Fig. 1), we cannot calculate its topographic profiles from the LOLA observations as we did for the Finsen crater. Here we just assume that the impact model could reasonably reproduce the similar-size structure of the Leibnitz crater and estimate its ejecta thickness along the radial distance from the crater centre. Supplementary Fig. 4b shows the ejecta thickness variation of the Leibnitz-sized crater along the radial distance beyond the crater. The Chang'E-4 landing site is ~230 km from the centre of the Leibnitz crater. According to our estimation, ejecta with a thickness of ~200 m from the Leibnitz crater deposited at the Chang'E-4 landing site.

Data availability

The data used in this work is available on the Science and Application Center for Moon and Deep Space Exploration, Chinese Academy of Sciences (http://moon.bao.ac.cn).

Code availability

The code for processing the LPR data is available from the corresponding author on request.

Received: 7 July 2019; Accepted: 3 August 2020;
Published online: 07 September 2020

References

1. Ohtake, M. et al. Geologic structure generated by large-impact basin formation observed at the South Pole–Aitken basin on the Moon. *Geophys. Res. Lett.* **41**, 2738–2745 (2014).
2. Melosh, H. J. et al. South Pole–Aitken basin ejecta reveal the Moon's upper mantle. *Geology* **45**, 1063–1066 (2017).
3. Moriarty, D. P. III & Pieters, C. M. The character of South Pole–Aitken basin: patterns of surface and subsurface composition. *J. Geophys. Res. Planets* **123**, 729–747 (2018).
4. Li, C. et al. Chang'e-4 initial spectroscopic identification of lunar far-side mantle-derived material. *Nature* **569**, 378–382 (2019).
5. Wu, W. et al. Lunar farside to be explored by Chang'e-4. *Nat. Geosci.* **12**, 222–223 (2019).
6. Stuart-Alexander, D. E. *Geologic Map of the Central Far Side of the Moon* Investigations Map Series I-1047 (USGS, 1978).
7. Peeples, W. J., Sill, W. R. & May, T. W. Orbital radar evidence for lunar subsurface layering in Maria Serenitatis and Crisium. *J. Geophys. Res. Solid Earth* **83**, 3459–3468 (1978).
8. Sharpton, V. L. & Head, J. W. Stratigraphy and structural evolution of southern Mare Serenitatis: a reinterpretation based on Apollo Lunar Sounder Experiment data. *J. Geophys. Res. Solid Earth* **87**, 10983–10998 (1982).
9. Ono, T. et al. Lunar radar sounder observations of subsurface layers under the nearside maria of the Moon. *Science* **323**, 909–912 (2009).
10. Shkuratov, Y. G., Kaidash, V. G., Kreslavsky, M. A. & Opanasenko, N. V. Absolute calibration of the Clementine UVVIS data: comparison with ground-based observation of the moon. *Sol. Syst. Res.* **35**, 29–34 (2001).
11. Petro, N. E. & Pieters, C. M. The lunar-wide effects of basin ejecta distribution on the early megaregolith. *Meteorit. Planet. Sci.* **43**, 1517–1529 (2008).
12. Heiken, G. H., Vaniman, D. T. & French, B. M. *Lunar Sourcebook: A User's Guide to the Moon* (Cambridge Univ. Press, 1991).

13. Montopoli, M., Tognolatti, P., Marzano, F. S., Pierdicca, M. & Perrotta, G. Remote sensing of the Moon sub-surface from a spaceborne microwave radiometer aboard the European Student Moon Orbiter (ESMO). In *Proc. IEEE International Geoscience and Remote Sensing Symposium (IGARSS)* 4451–4454 (2007).
14. Fa, W. Z. & Jin, Y. Q. A primary analysis of microwave brightness temperature of lunar surface from Chang'e-1 multi-channel radiometer observation and inversion of regolith layer thickness. *Icarus* **207**, 605–615 (2010).
15. Hawke, B. R. & Head, J. W. Impact melt on lunar crater rims. In *Impact and Explosion Cratering* (eds Roddy, D. J. et al.) 815–841 (Pergamon Press, 1977).
16. Wilcox, B. B., Lucey, P. G. & Gillis, J. J. Mapping iron in the lunar mare: an improved approach. *J. Geophys. Res. Planets* **110**, E11001 (2005).
17. Neish, C. D. et al. Spectral properties of Titan's impact craters imply chemical weathering of its surface. *Geophys. Res. Lett.* **42**, 3746–3754 (2015).
18. Zhang, J. H. et al. Volcanic history of the Imbrium basin: a close-up view from the lunar rover Yutu. *Proc. Natl Acad. Sci. USA* **112**, 5342–5347 (2015).
19. Xiao, L. et al. A young multilayered terrane of the northern Mare Imbrium revealed by Chang'e-3 mission. *Science* **347**, 1226–1229 (2015).
20. Choy, T. C. *Effective Medium Theory: Principles and Applications* (Oxford Univ. Press, 2015)
21. Huang, Q. & Wieczorek, M. A. Density and porosity of the lunar crust from gravity and topography. *J. Geophys. Res. Planets* **117**, E05003 (2012).
22. Olhoeft, G. R. & Strangway, D. W. Dielectical properties of the first 100 meters of the Moon. *Earth Planet. Sci. Lett.* **24**, 394–404 (1975).
23. Ivanov, M. A. et al. Geologic history of the northern portion of the South Pole–Aitken basin on the Moon. *J. Geophys. Res. Planets* **123**, 2585–2612 (2018).
24. Huang, J. et al. Geological characteristics of Von Kármán crater, northwestern South Pole–Aitken basin: Chang'e-4 landing site region. *J. Geophys. Res. Planets* **123**, 1684–1700 (2018).
25. Du, J. et al. Thickness of lunare mare basalts: new results based on modeling the degradation of partially buried craters. *J. Geophys. Res. Planets* **124**, 2430–2459 (2019).
26. Di, K. et al. Topographic evolution of Von Kármán crater revealed by the lunar rover Yutu-2. *Geophys. Res. Lett.* **46**, 12764–12770 (2019).
27. Li, C. et al. The Moon's farside shallow subsurface structure unveiled by Chang'e-4 lunar penetrating radar. *Sci. Adv.* **6**, eaay6898 (2020).
28. Moriarty, D. P. III & Pieters, C. M. The nature and origin of Mafic Mound in the South Pole–Aitken basin. *Geophys. Res. Lett.* **42**, 7907–7915 (2015).
29. McGetchin, T. R., Settle, M. & Head, J. W. Radial thickness variation in impact crater ejecta: implications for lunar basin deposits. *Earth Planet. Sci. Lett.* **20**, 226–236 (1973).
30. Fang, G. Y. et al. Lunar penetrating radar onboard the Chang'e-3 mission. *Res. Astron. Astrophys.* **14**, 1607–1622 (2014).
31. Su, Y. et al. Data processing and initial results of Chang'e-3 lunar penetrating radar. *Res. Astron. Astrophys.* **14**, 1623–1632 (2014).
32. Shen, S. et al. Design of dual-channel nonuniform digital sampling receiver for lunar penetrating radar in Chang'e-3 rover. *IEEE Aerosp. Electron. Syst. Mag.* **31**, 22–31 (2016).
33. Cagnoli, B. & Ulrych, T. J. Singular value decomposition and wavy reflections in ground-penetrating radar images of base surge deposits. *J. Appl. Geophys.* **48**, 175–182 (2001).
34. Di, K. C. et al. Chang'e-4 lander localization based on multi-source data. *J. Remote Sens.* **23**, 177–180 (2019).
35. Claerbout, J. F. *Imaging the Earth's Interior* (Blackwell Scientific, 1985).
36. Yilmaz, Ö. *Seismic Data Processing* (Society of Exploration Geophysicists, 1987).
37. Etgen, J., Gray, S. H. & Zhang, Y. An overview of depth imaging in exploration geophysics. *Geophysics* **74**, WCA5–WCA17 (2009).
38. Stoffa, P. L. et al. Split-step Fourier migration. *Geophysics* **55**, 410–421 (1990).
39. Wu, R. S. Wide-angle elastic wave one-way propagation in heterogeneous media and an elastic wave complex-screen method. *J. Geophys. Res.* **99**, 751–766 (1994).
40. Lv, W. et al. Comparative analysis of reflection characteristics of lunar penetrating radar data using numerical simulations. *Icarus* **350**, 113896 (2020).
41. Collins, G. S., Melosh, H. J. & Ivanov, B. A. Modeling damage and deformation in impact simulations. *Meteorit. Planet. Sci.* **39**, 217–231 (2004).
42. Wünnemann, K., Collins, G. S. & Melosh, H. J. A strain-based porosity model for use in hydrocode simulations of impacts and implications for transient-crater growth in porous targets. *Icarus* **180**, 514–527 (2006).
43. Amsden, A. A., Ruppel, H. M. & Hirt, C. W. *SALE: A Simplified ALE Computer Program for Fluid Flow at all Speeds* LANL Report LA-8095 (LANL, 1980).
44. Wünnemann, K., Zhu, M. H. & Stöffler, D. Impacts into quartz sand: crater formation, shock metamorphism, and ejecta distribution in laboratory experiments and numerical models. *Meteorit. Planet. Sci.* **51**, 1762–1794 (2016).
45. Melosh, H. J. et al. The origin of lunar mascon basins. *Science* **340**, 1552–1555 (2013).
46. Potter, R. W. K. et al. Constraining the size of the South Pole–Aitken basin impact. *Icarus* **220**, 730–743 (2012).
47. Potter, R. W. K. et al. Numerical modeling of the formation and structure of the Orientale impact basin. *J. Geophys. Res.* **118**, 963–979 (2013).
48. Zhu, M.-H., Wünnemann, K. & Potter, R. W. K. Numerical modeling of the ejecta distribution and formation of the Orientale basin on the Moon. *J. Geophys. Res.* **120**, 118–2,134 (2015).
49. Zhu, M. H. et al. Are the Moon's nearside-farside asymmetries the result of a giant impact? *J. Geophys. Res.* **124**, 2117–2140 (2019).
50. Ahrens, T. J. & O'Keefe, J. D. Shock melting and vaporization of lunar rocks and minerals. In *Impact and Explosion Cratering* (eds Roddy, D. J. et al.) 639–656 (Pergamon Press, 1977).
51. Benz, W., Cameron, A. G. W. & Melosh, H. J. The origin of the Moon and the single-impact hypothesis III. *Icarus* **81**, 113–131 (1989).
52. Wieczorek, M. A. et al. The crust of the Moon as seen by GRAIL. *Science* **339**, 671–675 (2013).
53. Ivanov, B. A., Melosh, H. J. & Pierazzo E. in *Large Meteorite Impacts and Planetary Evolution IV* (eds Gibson, R. L. & Reimold, W. U.) 29–49 (Geological Society of America, 2010).
54. Melosh, H. J. Acoustic fluidization: a new geologic process? *J. Geophys. Res.* **84**, 7513–7520 (1979).
55. Melosh, H. J. & Ivanov, B. A. Impact crater collapse. *Annu. Rev. Earth Planet. Sci.* **27**, 385–415 (1999).
56. Zhu, M. H., Wünnemann, K. & Artemieva, N. Effects of Moon's thermal state on the impact basin ejecta distribution. *Geophys. Res. Lett.* **44**, 11292–11300 (2017).
57. Bottke, W. F. et al. An Archaean heavy bombardment from a destabilized extension of the asteroid belt. *Nature* **485**, 78–81 (2012).
58. Le Feuvre, M. & Wieczorek, M. A. Nonuniform cratering of the Moon and a revised crater chronology of the inner Solar System. *Icarus* **214**, 1–20 (2011).
59. Hörz, F., Ostertag, R. & Rainey, D. A. Bunte Breccia of the Ries: continuous deposits of large impact crater. *Rev. Geophys. Space Phys.* **21**, 1667–1725 (1983).
60. Artemieva, N. A. et al. Ries crater and suevite revisited—observation and modeling. Part II: modeling. *Meteorit. Planet. Sci.* **48**, 590–627 (2013).
61. Stöffler, D. et al. Experimental hypervelocity impact into quartz sand: distribution and shock metamorphism of ejecta. *J. Geophys. Res.* **80**, 4062–4077 (1975).
62. Fortezzo, C. M. & Hare, T. M. Completed digital renovation of the 1:5,000,000 lunar geologic map series. *Lunar Planet. Sci. Conf.* **44**, 2623 (2013).

Acknowledgements

The Chang'E-4 mission was carried out by the Chinese Lunar Exploration Program, and the data were provided by the China National Space Administration. We thank D. Moriarty for helpful suggestions, which greatly improved the clarity and readability of the manuscript. This work was supported by Key Research Program of Frontier Sciences, Chinese Academy of Sciences (QYZDJ-SSW-DQC001) and the National Nature Science Foundation of China (41490631 and 41941002). M.-H.Z. was supported by the Science and Technology Development Fund, Macau (0079/2018/A2) and the pre-research project on Civil Aerospace Technologies No. D020202 funded by China National Space Administration (CNSA). M.-H.Z. acknowledges the iSALE developers. H.S. was supported by the Beijing Municipal Science and Technology Commission (Z181100002918003) and the pre-research project on Civil Aerospace Technologies No. D020201 funded by China National Space Administration (CNSA). We thank the Supercomputing Laboratory of IGGCAS for providing computing resources.

Author contributions

Yangting Lin lead the study; J.Z., B.Z., Yangtin Lin, H.S., Yi Lin, C.L. and Z. Yao processed and analysed the LPR data; Yangting Lin, M.-H.Z., J.Z., W.Y., K.D., Z. Yue and Z.O. interpreted the lunar geology; M.-H.Z. simulated impacting; B.Z., Z.D., Y.G., H.L., J.Y., E.L. and L.W. designed the payloads; Yangting Lin, J.Z., M.-H.Z. and H.S. prepared the manuscript.

Competing interests

The authors declare no competing interests.

Additional information

Extended data is available for this paper at https://doi.org/10.1038/s41550-020-1197-x.

Supplementary information is available for this paper at https://doi.org/10.1038/s41550-020-1197-x.

Correspondence and requests for materials should be addressed to Y.L.

Peer review information *Nature Astronomy* thanks Gareth Morgan and the other, anonymous, reviewer(s) for their contribution to the peer review of this work.

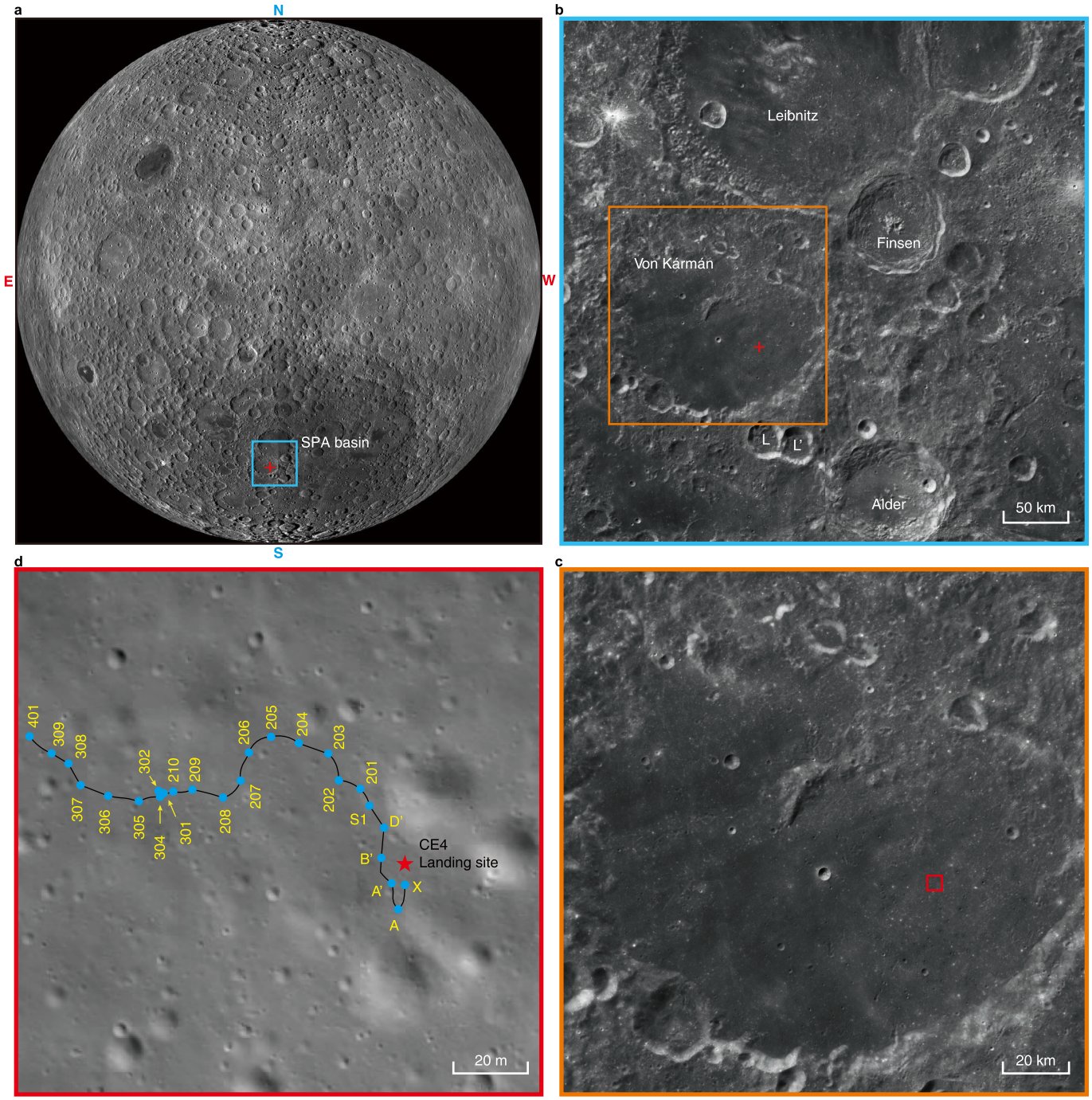

Extended Data Fig. 1 | The location of Chang'E-4 landing site and the track of Yutu-2 rover. a, The farside of the Moon; **b**, Local details in the rectangle in **a**; **c**, Local details in the rectangle in **b**; **d**, Local details in the rectangle in **c**. **a** is obtained by the Lunar Resonant Orbiter (http://lroc.sese. asu.edu/posts/298); **b** and **c** are obtained by Chang'E-2 (http://moon.bao.ac.cn); **d** is obtained by the descending camera under the Chang'E-4 lander.

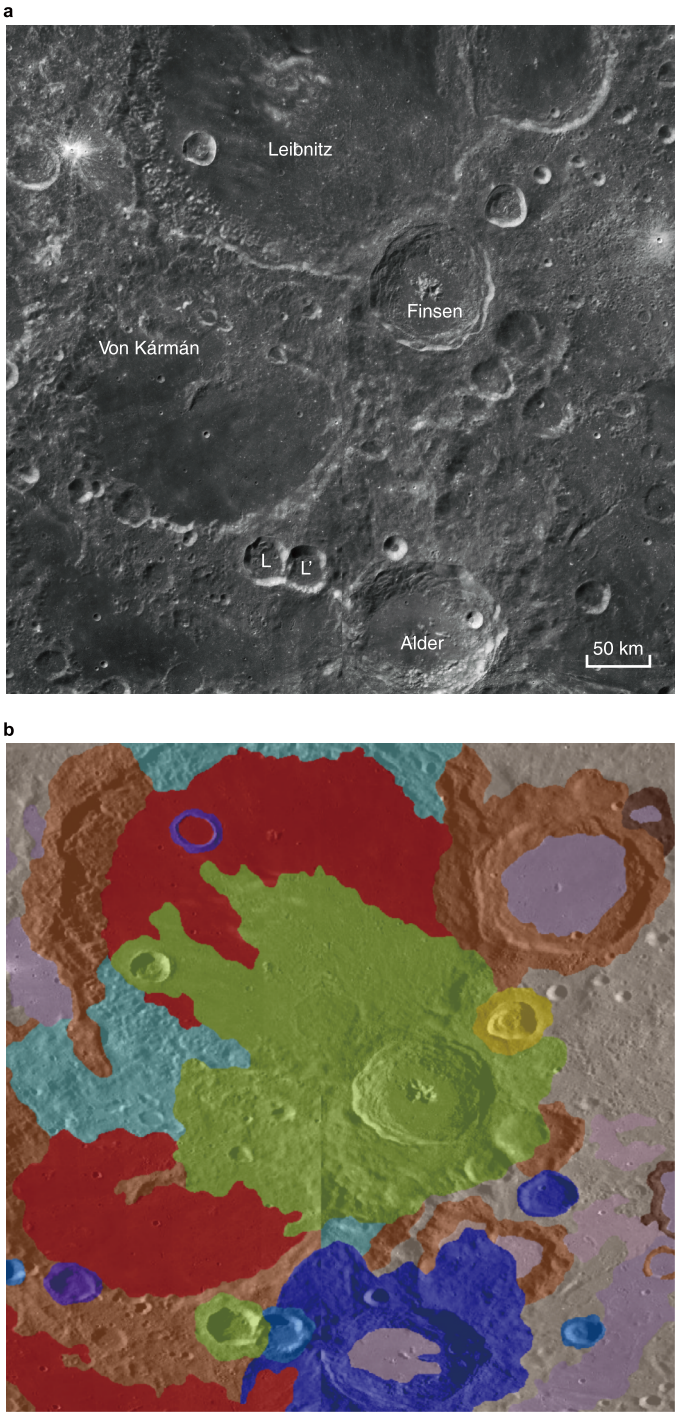

Extended Data Fig. 2 | High resolution image of the Chang'E-4 landing site and the regional geology. a, The Chang'E-4 landing site; **b**, The regional geology that modified from https://quickmap.lroc.asu.edu [62].

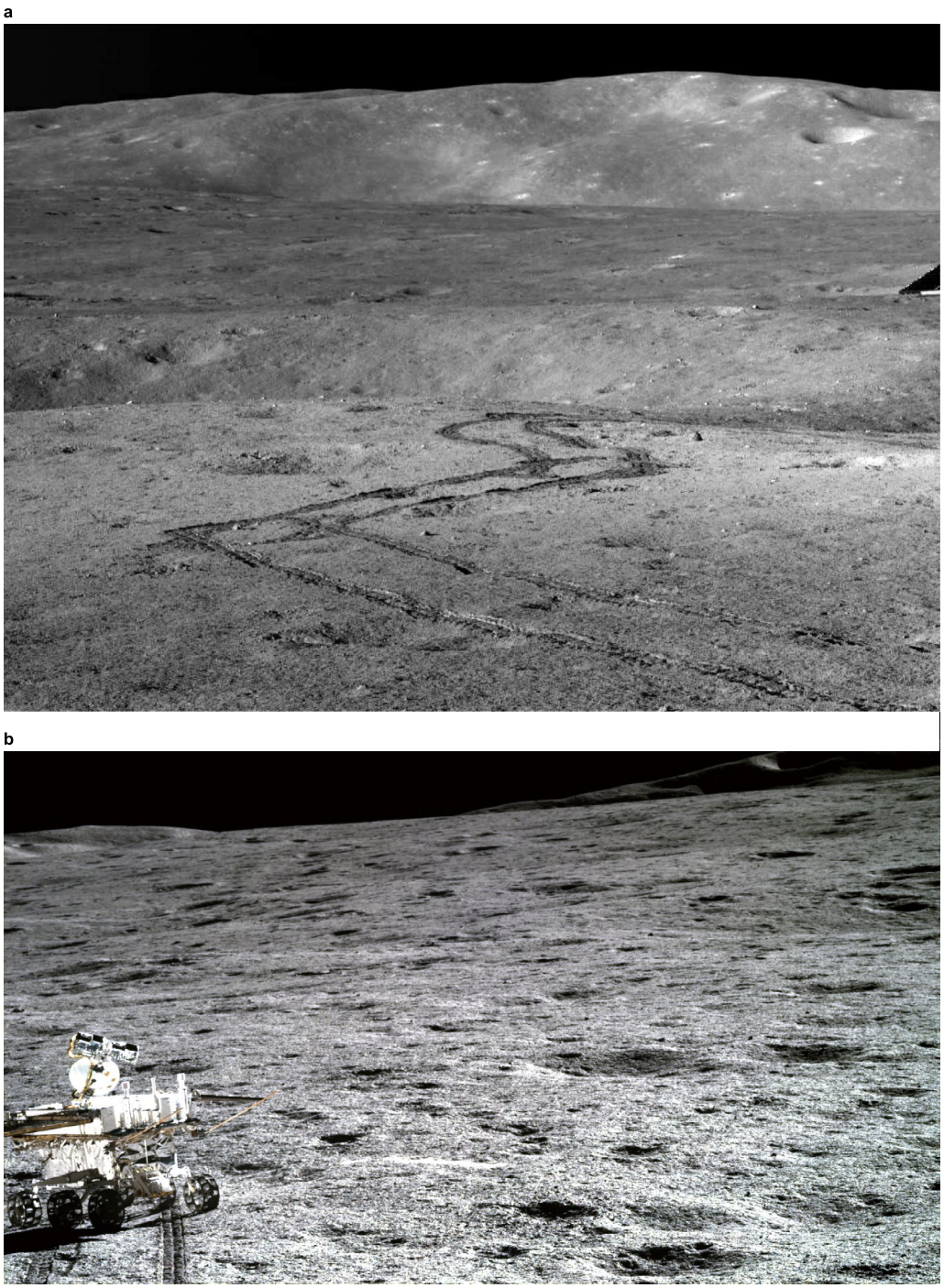

Extended Data Fig. 3 | The rareness of rocks on the lunar surface at the Chang'E-4 landing site. The landscape images were taken with the panorama camera on the rover Yutu-2 (**a**) and by the terrain camera on the Chang'E-4 lander (**b**). The distance between two rows of wheels is ~80 cm.

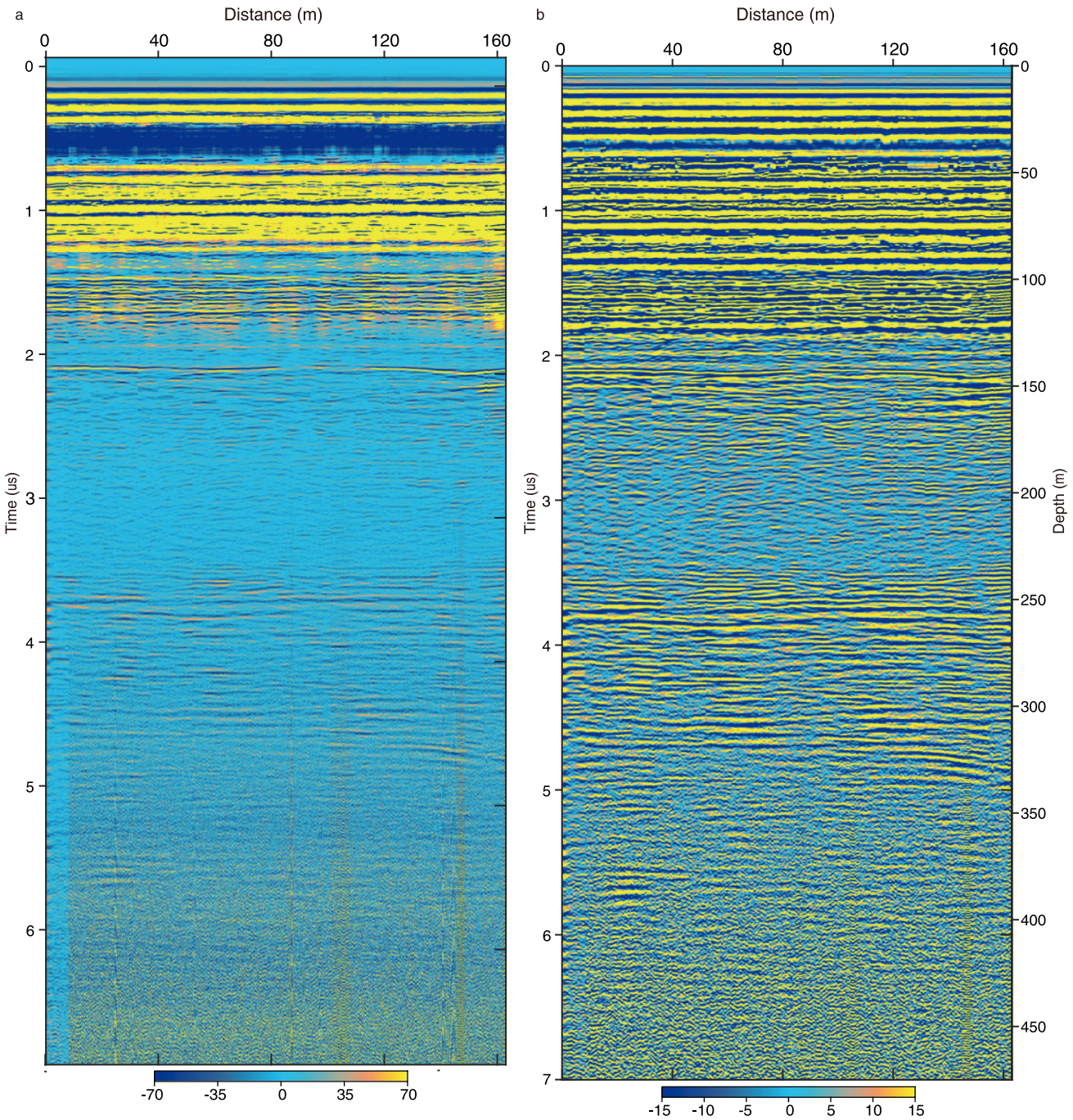

Extended Data Fig. 4 | The LPR data of Channel-1. a, The raw data profile; **b**, The profile after using a bandpass filter between 10 and 80 MHz for each trace and a 2D median filter using parameters of (3,10). The depth is converted from the travel time using a relative dielectric model shown in Extended Data Fig. 7. The processed data shown in **b** is exactly the same as that shown in Fig. 2, which is shown here to examine the processing results compared with the original data shown in **a**.

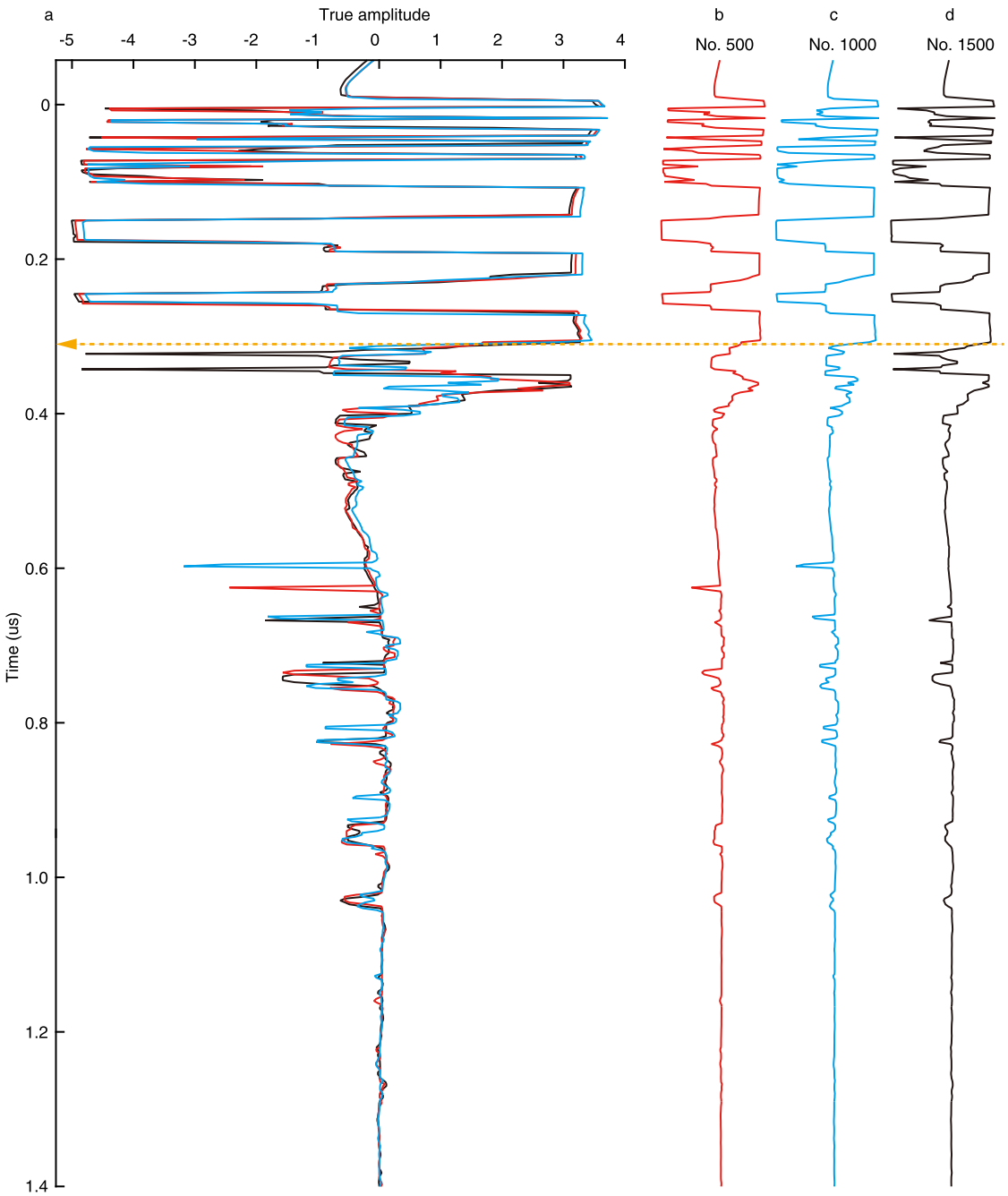

Extended Data Fig. 5 | Local zoom in of original waveforms of low-frequency LPR Channel from 0 to 1.4 μs. a, The stack of three waveforms at the trace no. 500, 1000, and 1500. **b**, **c**, **d**, The independent waveforms at trace no. 500, 1000, and 1500, respectively. Note that only the waveforms within 0.31 μs (indicated by the orange arrow) have been apparently clipped and the rest are reliable.

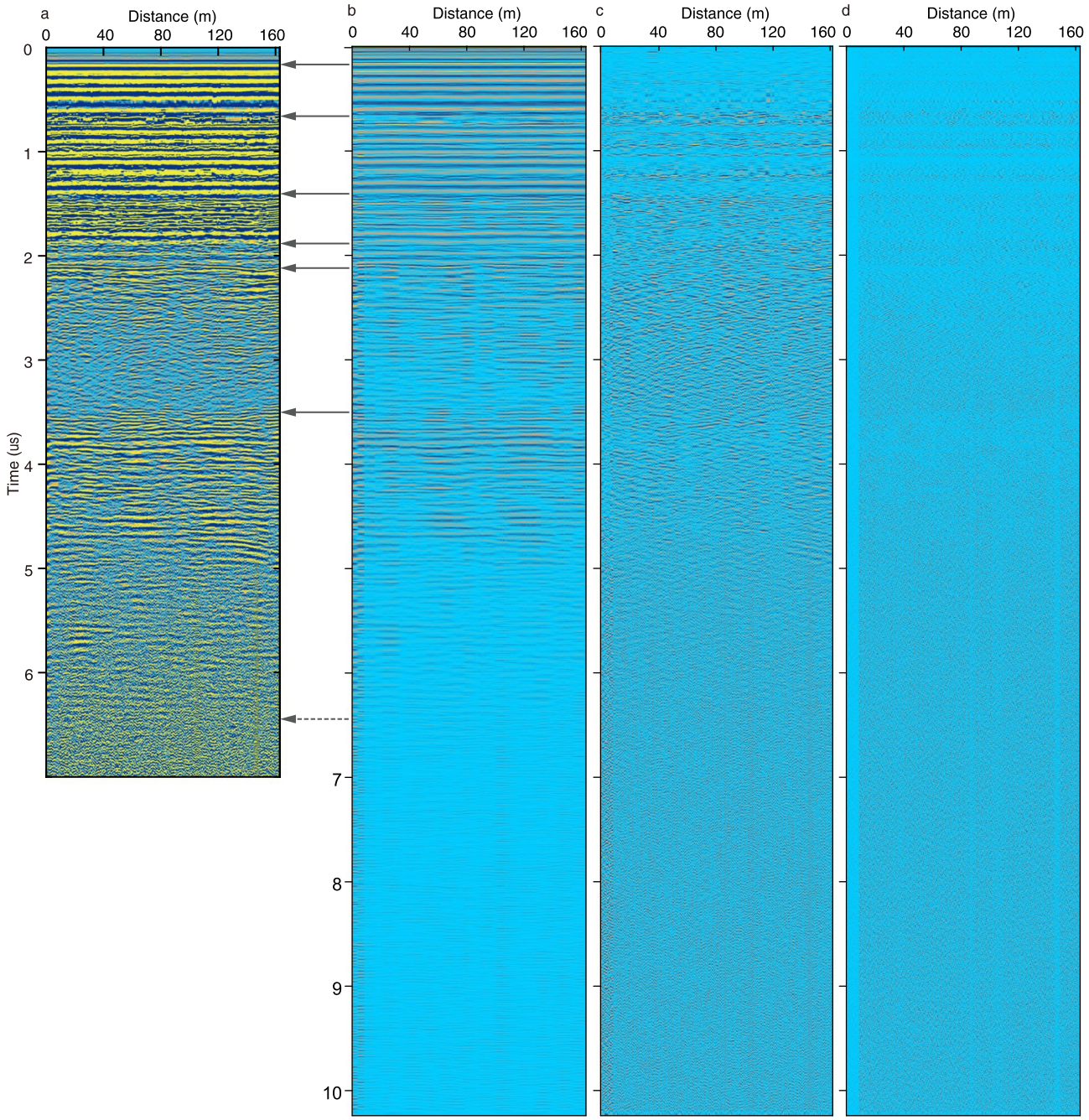

Extended Data Fig. 6 | Singular value decomposition of low-frequency channel. a, The same profile as shown in Fig. 2. **b**, The low-pass eigenimage[33] (only keeping eigenvalues from 1 to 10); **c**, the band-pass eigenimage (only keeping eigenvalues from 11 to 200); **d**, the high-pass eigenimage (only keeping eigenvalues from 201 to 1973). **b**-**d** share the same color scale but is slightly less clipped than **a** for the convenience of pattern comparison. The singular values are shown in Supplementary Fig. 5.

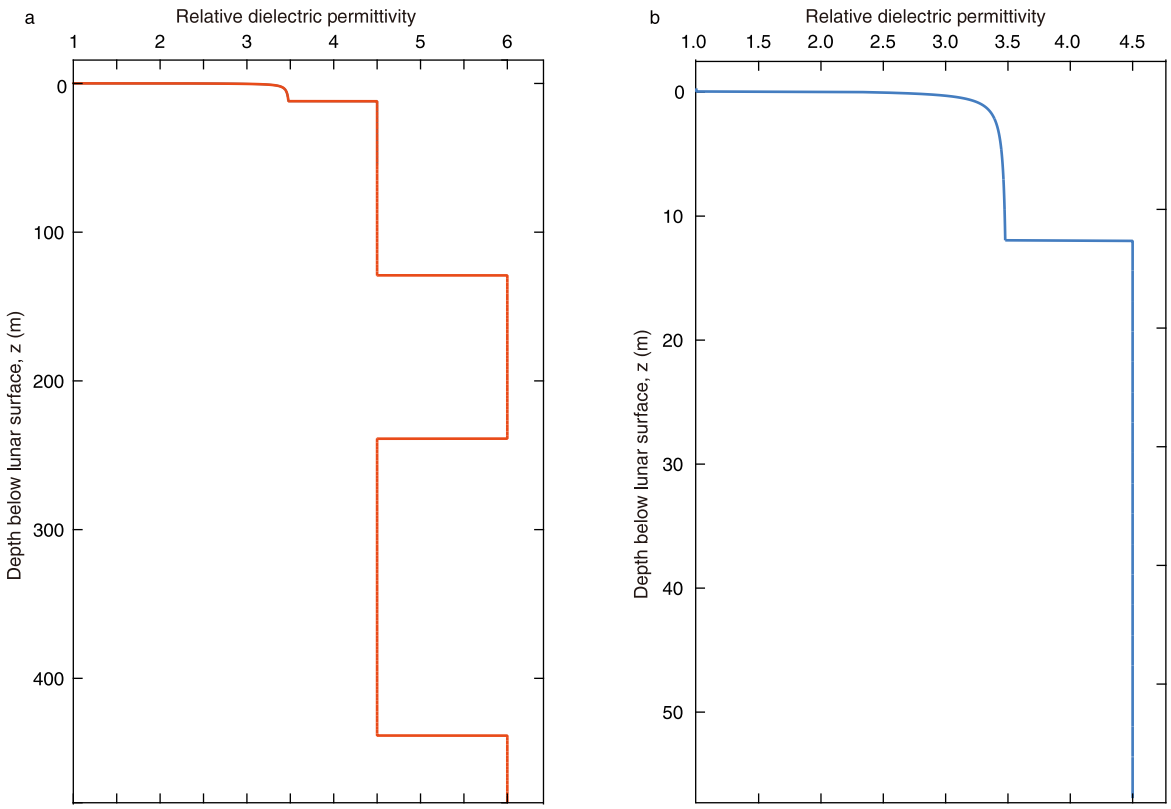

Extended Data Fig. 7 | The lunar regolith model of the relative dielectric constant. a, The whole model; **b**, Local details of **a** within 60 m. This model is constructed after the Apollo samples[12], which can be used to convert the travel time to depth in Fig. 2 and Extended Data Fig. 4.

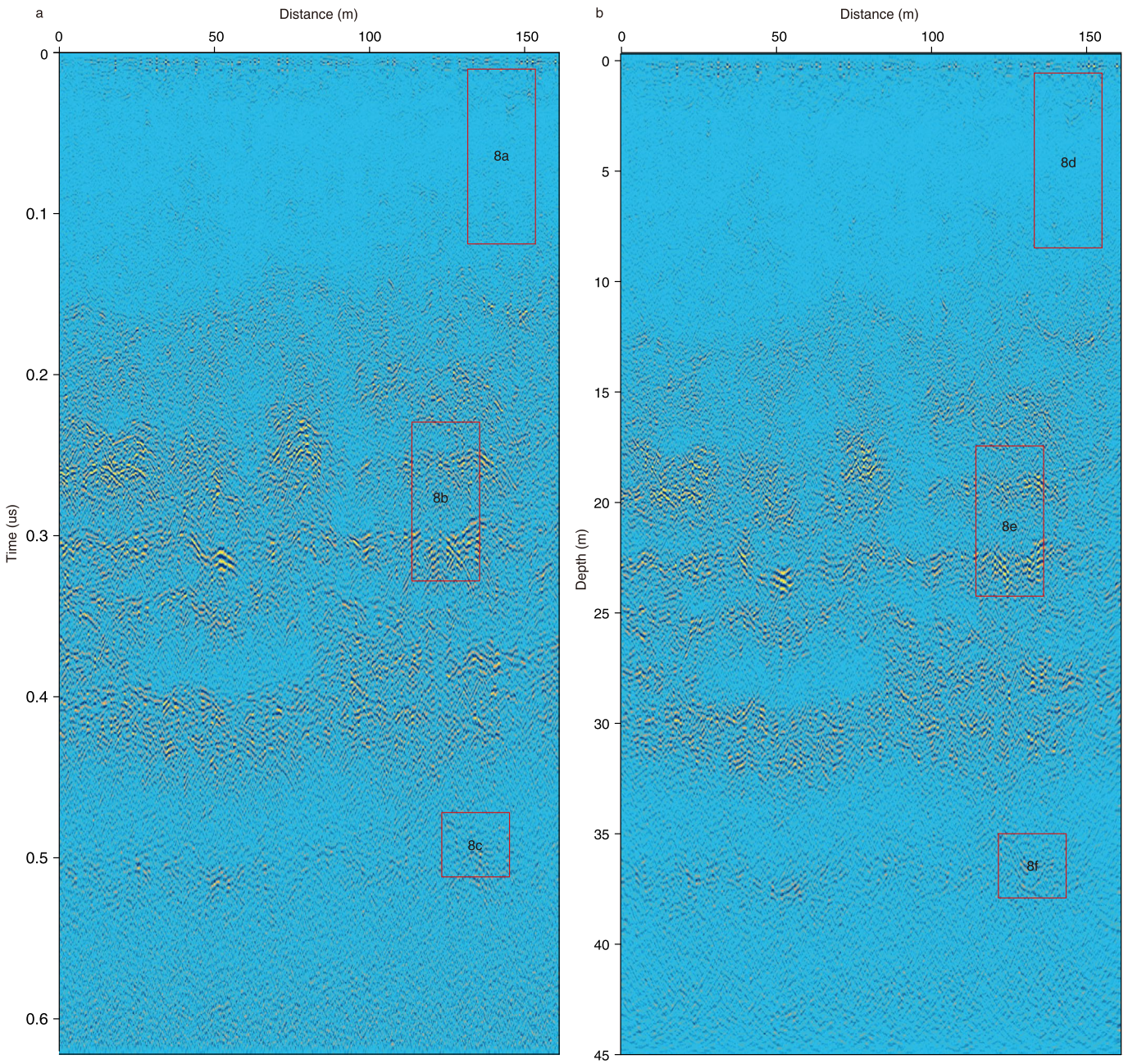

Extended Data Fig. 8 | Comparison between the original LPR profile and the migration result. a, The original LPR profile; **b**, The migration result. The data are obtained by the high-frequency Channel-2B. The local details in the rectangles are shown in Extended Data Fig. 9.

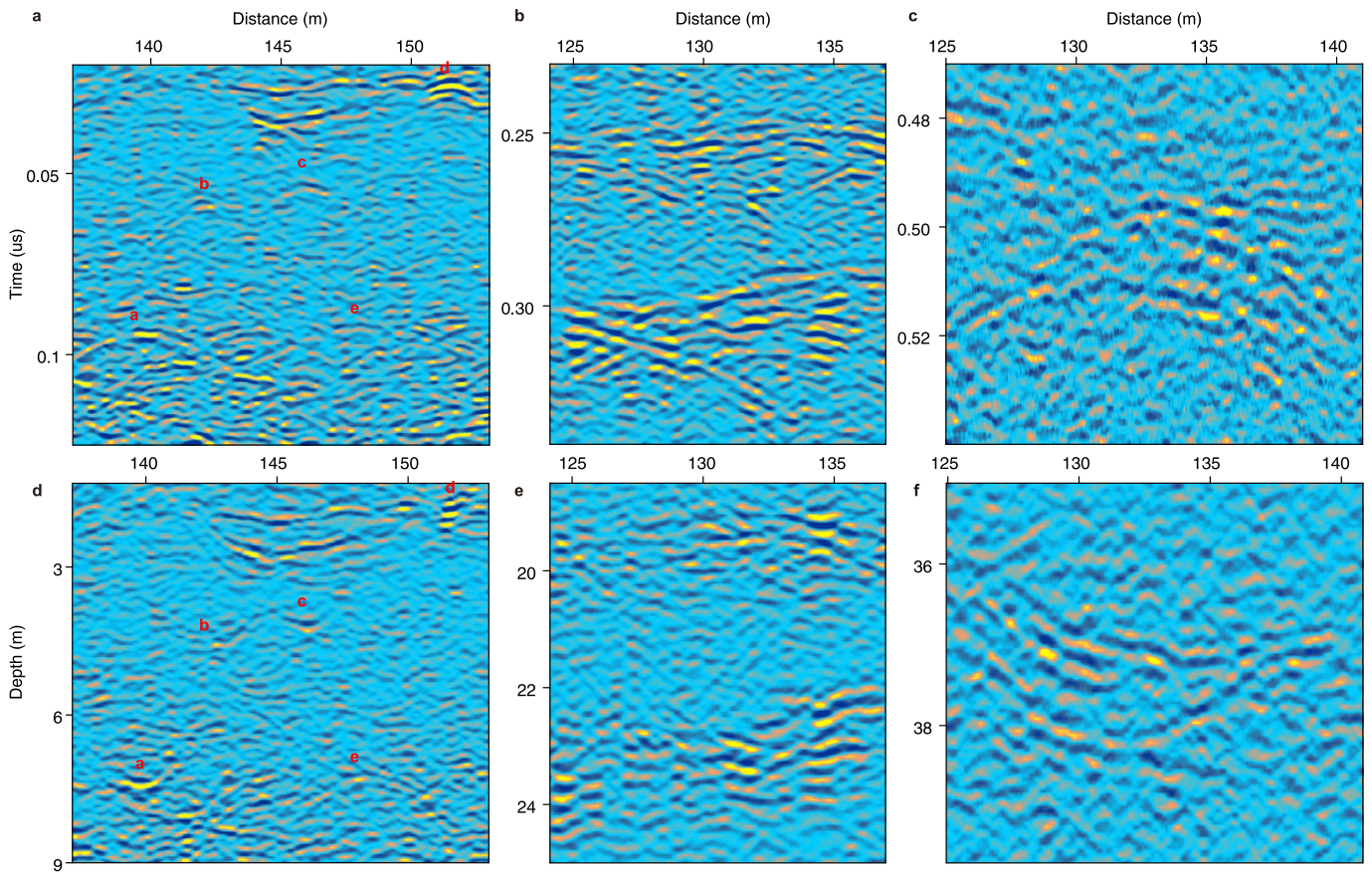

Extended Data Fig. 9 | Local details in the rectangles in Extended Data Fig. 8. a–c, The original LPR profiles; **d–f**, The corresponding migration results of **a–c**, respectively.

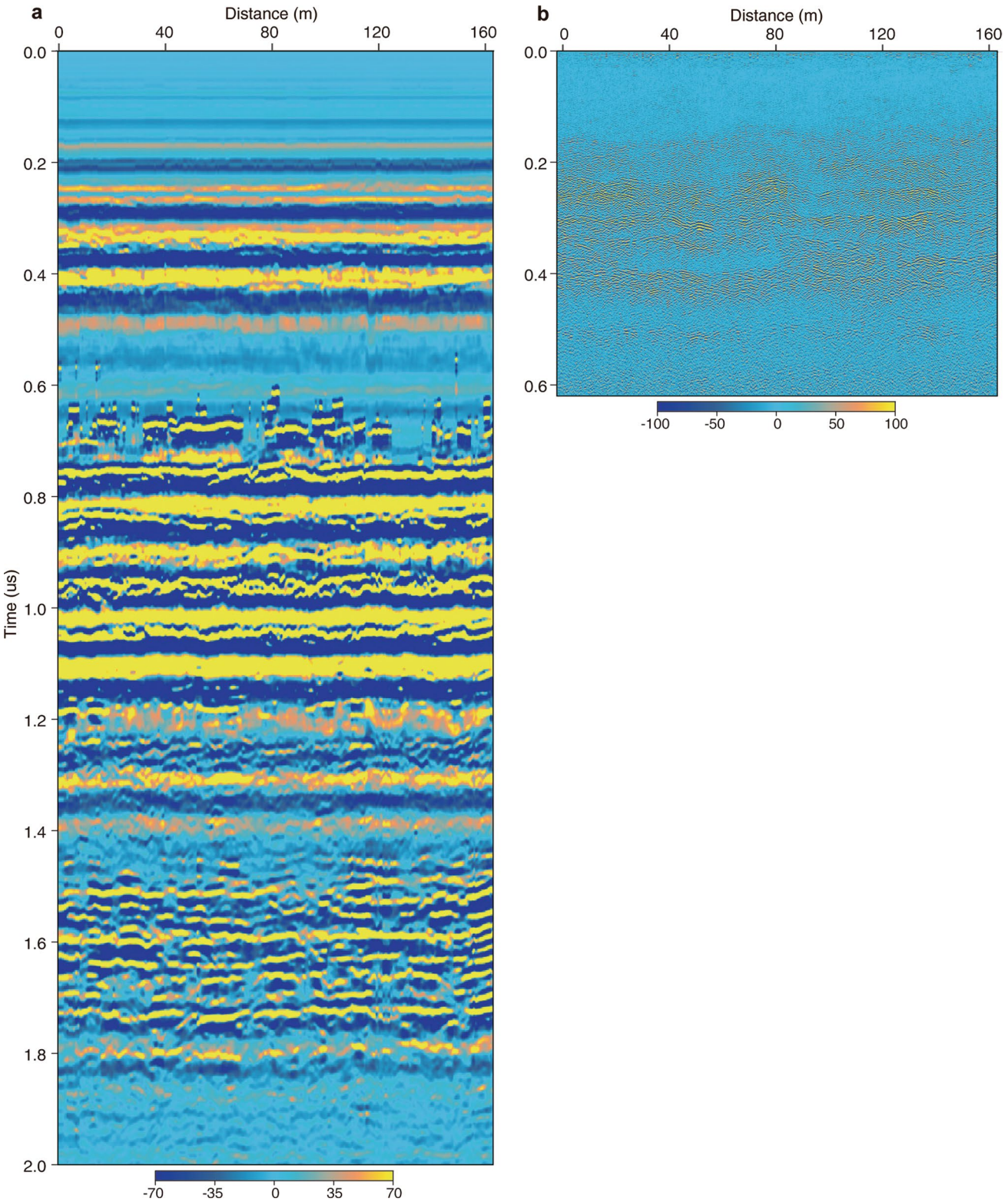

Extended Data Fig. 10 | Comparison between the low-frequency and high-frequency LPR channels. a, Low-frequency channel; **b**, High-frequency channel. The high-frequency channel can well constrain the subsurface structures within 0.62 μs.